Research Square

Preprints are preliminary reports that have not undergone peer review.
They should not be considered conclusive, used to inform clinical practice,
or referenced by the media as validated information.

Built-in electric field-boosted attomolar Pb^{2+} sensing on carboxylated black phosphorene

Leiming Wu
leiming_wu@gdut.edu.cn
Guangdong University of Technology
Fan Yang
Guangdong University of Technology
Xixi Yuan
Guangdong University of Technology
Jiaqi Zhu
Guangdong University of Technology
Yuanyuan Pan
Macau University of Science and Technology
Zhongjun Li
Macau University of Science and Technology
Jianqing Li
Macau University of Science and Technology https://orcid.org/0000-0002-6768-1483
Yanqi Ge
Shenzhen University
Yuanjiang Xiang
Hunan University https://orcid.org/0000-0003-0411-2029
Han Zhang
Shenzhen University https://orcid.org/0000-0002-3185-5680
Jun Yang
Guangdong University of Technology
Yuwen Qin
Guangdong University of Technology https://orcid.org/0000-0001-9879-1514

Article

Keywords: carboxylated black phosphorene, built-in electric field, high selectivity, attomolar lead ion detection

Posted Date: June 2nd, 2026

DOI: https://doi.org/10.21203/rs.3.rs-9871587/v1

License: This work is licensed under a Creative Commons Attribution 4.0 International License.
Read Full License

Additional Declarations: There is **NO** Competing Interest.

Version of Record: A version of this preprint was published at Nature Communications on September 14th, 2026. See the published version at https://doi.org/10.1038/s41467-026-77793-6.

Abstract

Lead ion (Pb^{2+}) contamination poses a severe and persistent threat to environmental safety and human health, demanding ultrasensitive and selective detection strategies. Herein, we fabricate a carboxyl-functionalized black phosphorene modified surface plasmon resonance sensor (SPR+BP-COOH) with built-in electric field enhancement for attomolar-level and highly selective Pb^{2+} detection. The Au/BP-COOH junction generates a strong interfacial built-in electric field, which markedly strengthens near-field electromagnetic coupling and amplifies the SPR optical response, thereby significantly boosting detection sensitivity. Meanwhile, abundant oxygen-containing sites on BP-COOH enable efficient and specific adsorption of Pb^{2+}. Impressively, this sensor achieves an ultralow detection limit of 10^{-19} M, 13 orders of magnitude lower than that of bare Au-SPR, and exhibits outstanding selectivity against Cd^{2+}, Cu^{2+}, Zn^{2+}, Ni^{2+}, Ca^{2+}, and Mg^{2+}. This label-free and straightforward platform provides a reliable route for ultratrace heavy-metal monitoring in environmental and food-safety applications.

Introduction

Lead contamination remains a persistent environmental and public-health concern. Recent high-level assessments have shown that toxic metal pollution has become a global threat to agricultural sustainability, food safety, and human health [1–3]. Importantly, the risk is not limited to heavily polluted scenarios. Recent evidence indicates that even when heavy-metal concentrations in food formally satisfy existing regulatory thresholds, the corresponding dietary intake may still impose non-negligible health risks [4]. Within this broader context, Pb^{2+} remains particularly concerning because of its persistence across water–soil–food systems, its continuing exposure burden in modern populations, and its well-established toxicity to neurological and developmental health [5–7]. These considerations continue to motivate the development of analytical strategies capable of identifying Pb^{2+} at extremely low concentrations.

A central difficulty in Pb^{2+} monitoring is that environmentally relevant exposure may arise from long-term, low-level, and mixed-source conditions rather than only from highly contaminated samples. Recent work on chemical exposure through drinking water has further emphasized that analytical monitoring must increasingly address low-abundance contaminants in complex exposure pathways [8]. For Pb^{2+}, this requirement places particular pressure on sensing platforms to combine high sensitivity with simple operation and reliable interfacial readout. In practice, a desirable Pb^{2+} sensor should not only provide a low limit of detection, but should also maintain a direct and interpretable signal-transduction mechanism on a stable sensing interface.

Substantial progress has been made in Pb^{2+} sensing over the past decade. Fluorescent probes, colorimetric platforms, electrochemical sensors, and photoelectrochemical strategies have all been developed to improve sensitivity through molecular recognition and signal amplification [9–13]. Fluorescence-based methods offer convenient optical readout and have reached low concentration regimes through probe engineering. For example, a single-labeled fluorescent oligonucleotide probe

enabled Pb^{2+} detection down to 96 pmol/L, whereas a peptide-based ratiometric fluorescent probe reported a limit of detection of 3.8 nM [9,10]. Electrochemical and photoelectrochemical approaches can be pushed further when coupled with DNAzyme cleavage or amplification cascades. A single-step DNAzyme electrochemical sensor achieved a limit of detection of 1.26 fM, and a homogeneous dual-amplification electrochemical biosensor further reported 16.7 fM Pb^{2+} analysis, while a recent DNAzyme-assisted photoelectrochemical platform operated at 16.67 pmol/L [11–13]. These studies clearly demonstrate that ultra-trace Pb^{2+} analysis is achievable. However, many of these platforms rely on labels, multistep reaction schemes, or amplification modules that are not intrinsic to the sensing interface itself. For a conventional optical platform that reads out surface events directly and in real time, achieving such low concentration detection remains substantially more challenging.

Surface plasmon resonance (SPR) is especially attractive in this regard because it provides a label-free method for converting local refractive-index perturbations at a metal interface into measurable optical signals [14–16]. Since the first demonstration of SPR sensing in the early 1980s [14], and its subsequent development into a widely used analytical technology [15], prism-coupled SPR has become a central tool for interfacial analysis in chemistry, biology, and materials science. A recent authoritative primer further emphasized that prism-coupled SPR remains the most broadly used configuration for in situ monitoring of thin films, molecular adsorption, and interfacial interactions [16]. These features are directly relevant to metal-ion detection because they allow the sensing event to be read from the interface itself, without fluorescent tags or electrochemical mediators.

Despite these advantages, bare-Au SPR remains intrinsically challenged for Pb^{2+} sensing. The first challenge is physical: small ions induce only weak interfacial refractive-index perturbations, so the corresponding resonance-angle shift is often limited at low concentration. The second challenge is chemical: if the metal surface lacks favorable binding sites, the interfacial response to Pb^{2+} can remain weak and insufficiently differentiated from that of other ions. Existing Pb^{2+} SPR studies have partially addressed these issues through DNAzyme-assisted recognition, nanoparticle conjugation, or alternative assay configurations [17–19]. For example, a label-free SPR sensor based on DNAzyme–gold nanoparticle conjugates reported an 80 pM detection limit, and an SPR-based assay kit achieved 1 nM detection, whereas a fiber-based SPR configuration operated at approximately 4.8×10^{-9} M [17–19]. Earlier amplified SPR work based on a Pb^{2+}-dependent DNAzyme and a hemin/G-quadruplex label reported 5 fM detection, but this relied on an amplification strategy rather than a simple direct interfacial design [20]. Together, these studies improved SPR performance, but they also illustrate the general difficulty of pushing a SPR platform toward ultra-trace Pb^{2+} detection while preserving structural simplicity. In particular, the concentration regimes accessible to reported Pb^{2+} SPR systems still remain substantially higher than those reached by highly amplified electrochemical routes [11,12].

One promising way to overcome this limitation is to engineer the plasmonic interface with an ultrathin functional layer. In this strategy, the overlayer is expected to do more than simply decorate the surface. It should simultaneously amplify the effective optical perturbation experienced by the plasmonic field and provide chemically favorable sites for target binding. Two-dimensional materials are appealing in this

context because they combine atomic-to-nanoscale thickness, high surface exposure, and tunable interfacial chemistry, and recent analyses of 2D material-based SPR biosensors further underscore the value of such ultrathin interfacial layers for sensitivity enhancement [21,27]. Representative recent studies have also shown that highly active 2D recognition surfaces can enable attomolar-level metal-ion detection when the interfacial chemistry is appropriately designed [22,23]. These advances underscore an important principle: the sensing limit is not determined only by the transducer itself, but also by how efficiently the interface converts analyte binding into an optical or electrical perturbation.

Among the available 2D materials, BP is especially attractive for plasmonic sensing because of its distinctive electronic structure and strong surface sensitivity [24,25]. Since its emergence as a 2D electronic material with unusual optoelectronic properties [24], BP has been widely recognized as a promising platform for sensing applications [25,28]. At the same time, its practical use depends strongly on interfacial regulation. BP is chemically reactive and prone to degradation under ambient conditions, so protective or functional surface chemistry is often essential for stabilizing the material and making its reactivity analytically useful [26]. In the SPR field, previous studies have already suggested that few-layer BP can improve angular sensitivity by modifying the interfacial optical field and coupling characteristics [27,29]. More recent progress in solution-processable 2D material inks also supports the broader feasibility of constructing functionalized ultrathin 2D interfaces for device applications [30]. Together, these developments make BP a strong candidate for building an SPR interface that is both optically responsive and chemically addressable.

Here, we construct a built-in electric field-enhanced SPR + BP-COOH by directly stacking a BP-COOH functional layer onto a prism-coupled Au-film SPR platform. In this design, the BP layer is intended to enhance the angular SPR response, while the oxygen-containing chemical environment of the BP-COOH functional layer provides favorable interfacial sites for Pb^{2+} interaction. Unlike recognition strategies that depend on DNAzymes, labels, or multistep amplification reactions, this structure retains the simplicity of a bare-Au SPR platform while directly engineering the sensing interface itself. Under the same sensing framework, the limit of detection for Pb^{2+} reaches 10^{-19} M for the proposed built-in electric field-enhanced SPR + BP-COOH, whereas bare-Au SPR detects Pb^{2+} only down to 10^{-6} M. This study develops a simple yet effective modification route, which advances SPR sensing for ultratrace Pb^{2+} monitoring.

Results

Interfacial structure and proposed Pb^{2+} recognition pathway of SPR + BP-COOH. As illustrated in Fig. 1, a SPR sensor modified with BP-COOH was constructed by depositing a BP-COOH functional layer onto a prism-coupled Au film. The BP-COOH nanosheets were obtained by liquid-phase exfoliation of bulk BP followed by PEI/PAA functionalization, which introduced oxygen-containing surface groups to the nanosheet interface. In the resulting SPR + BP-COOH structure, the BP-COOH functional layer serves as the recognition-active interface, while the underlying Au film serves as the plasmonic transduction layer. According to the schematic shown in Fig. 1, carboxylate O sites are expected to be the major interaction sites for Pb^{2+}, whereas oxidized P–O sites may provide an auxiliary contribution.

On this basis, the selective interaction mechanism of Pb^{2+} at the BP-COOH interface can be described by the following interfacial reactions:

$$BP\text{-}COOH \rightleftharpoons BP\text{-}COO^- + H^+ \quad (1)$$

$$2(BP\text{-}COO^-) + Pb^{2+} \rightleftharpoons (BP\text{-}COO)_2Pb \quad (2)$$

These equations are used here to describe a plausible oxygen-site-mediated interfacial pathway for BP-COOH. A related mechanistic logic has been discussed for Pb(II) uptake on other oxygen-containing two-dimensional surfaces, where hydroxyl-related ion-exchange behavior was considered, the surface process was written in explicit reaction form, and the corresponding XPS results were consistent with strong Pb interaction with O-containing sites [31]. Although the surface chemistry in that system is different from that of BP-COOH, this provides one useful basis for expressing the present Pb^{2+} interaction in reaction form. Under this proposed pathway, Pb^{2+} interaction with the BP-COOH functional layer perturbs the local interfacial refractive index and leads to a resonance-angle shift in the SPR response, as schematically shown in Fig. 1.

To examine the structural basis and chemical plausibility of this proposed oxygen-site-mediated pathway, the SPR + BP-COOH interface was characterized before and after Pb^{2+} exposure by AFM, STEM image, EDS elemental maps, and XPS. As shown in Fig. 2a, AFM confirms that the Au surface is covered by an ultrathin BP-COOH functional layer with a thickness of approximately 13 nm, which was used as the representative structure in the main-text sensing experiments. Before Pb^{2+} exposure, the STEM image in Fig. 2b together with the EDS elemental maps in Fig. 2c–f shows the presence of C, O and P on the nanosheet-covered region, while no obvious Pb signal is detected. After Pb^{2+} exposure, the nanosheet-covered morphology is retained in Fig. 2g, and the corresponding EDS elemental maps in Fig. 2h–k show the coexistence of C, O, P and Pb, indicating that Pb-containing species are present on the BP-COOH-modified interface.

The XPS results in Fig. 2l, m further support this interfacial evolution. Before reaction, the O 1s spectrum contains P–O and O = C–O components, while the C 1s spectrum shows C–C, C–O and O = C–O contributions, consistent with the presence of the BP-COOH functional layer on the Au surface. The P 2p region is located in the range of oxidized phosphorus species, and the Au 4f doublet from the underlying Au film remains clearly visible. No obvious Pb 4f signal is observed before Pb^{2+} exposure. After reaction, the C 1s spectrum remains dominated by C–C, C–O and O = C–O components, indicating that the BP-COOH functional layer is preserved, whereas the O 1s spectrum shows an additional Pb–O-related component together with the original P–O and O = C–O signals. At the same time, a distinct Pb 4f doublet assigned to Pb $4f_{5}/_{2}$ and Pb $4f_{7}/_{2}$ appears after reaction. The P 2p envelope remains mainly associated with oxidized phosphorus species before and after Pb^{2+} exposure. Taken together, the emergence of Pb in the EDS elemental maps, the appearance of Pb 4f, and the Pb–O-related component in O 1s are consistent with Pb^{2+} interaction with oxygen-containing sites in the BP-COOH functional layer.

Overall, Fig. 1 and Fig. 2 are used together to clarify the interfacial structure and proposed recognition mechanism of SPR + BP-COOH. Figure 1 defines the architecture of the sensing interface and gives a chemically reasonable description of Pb^{2+} interaction at oxygen-containing sites, whereas Fig. 2 provides morphological, elemental and chemical-state evidence that the BP-COOH functional layer is successfully formed on the Au film and undergoes corresponding interfacial changes after Pb^{2+} exposure. These results establish the structural and mechanistic basis for the subsequent analysis of sensitivity enhancement and Pb^{2+} sensing performance.

Optical basis and physical interpretation of sensitivity enhancement by the BP overlayer. To clarify the optical basis for the improved sensing performance of SPR + BP-COOH, the angular SPR responses of the Au-film structure with and without a BP overlayer were simulated by the transfer matrix method (TMM) [32], and the detailed calculation parameters are provided in Methods. As shown in Fig. 3a, b, when the refractive index of the sensing medium increases from n = 1.330 to 1.350, the reflectance minima of both structures shift toward larger incident angles. However, after introducing the BP layer, the resonance-angle displacement becomes markedly larger. For the bare-Au SPR structure with L = 0, the simulated resonance dips exhibit a relatively limited angular shift over this refractive-index range (Fig. 3a). In contrast, for the BP-modified structure with L = 8, the resonance-angle shift becomes much more pronounced under the same refractive-index variation (Fig. 3b), indicating that the BP overlayer can amplify the angular response of the SPR system to interfacial refractive-index perturbation. The layer-number dependence of this behavior is summarized in Fig. 3e. With increasing layer number, both the simulated angular sensitivity and the total resonance-angle shift first increase and then decrease. The angular sensitivity increases from 140 deg/RIU for bare-Au SPR to 265 deg/RIU at L = 8, while the corresponding angle shift also reaches its maximum in the same range. When the layer number is further increased, the response begins to decline, indicating that the effect of the BP overlayer is thickness dependent rather than monotonically increasing.

The corresponding near-field response is shown in Fig. 3c, d. The normalized electric-field intensity distribution was calculated at n = 1.33. For L = 0, the field intensity reaches its maximum near the Au/sensing-medium interface (Fig. 3c). For L = 8, the peak field intensity becomes higher and the high-field region near the interface becomes more pronounced (Fig. 3d). These results indicate that the stronger angular response of the L = 8 structure is accompanied by a more pronounced interfacial near-field enhancement.

The physical origin of this enhanced near-field response is schematically summarized in Fig. 4. As illustrated in Fig. 4a,b, the introduction of BP changes the interfacial optical environment of the Au-film SPR structure. BP possesses a relatively high refractive index over a broad spectral range, and its introduction onto the Au surface creates a stronger dielectric contrast at the plasmonic interface. Under this condition, the effective mode volume of the evanescent field is compressed, and the electromagnetic field becomes more strongly localized near the sensing interface. In addition, the multilayer structure of BP introduces interlayer coupling, which further enhances optical confinement and contributes to a stronger near-field response than that of the Au/sensing-medium structure.

A second contribution is illustrated in Fig. 4c, d. Because Au and BP have different work functions, contact between the two components can drive directional interfacial charge redistribution. This process leads to the formation of a built-in electric field at the Au/BP interface, which can further strengthen local electromagnetic coupling near the sensing region. In this sense, the role of BP in improving SPR sensitivity is not limited to adding an ultrathin overlayer, but also involves interfacial regulation of the local field environment. BP also exhibits a high carrier mobility, reported up to approximately 10^3 $cm^2/(V·s)$ at room temperature [24], which is favorable for efficient interfacial charge response. Taken together, the high-index confinement effect, multilayer coupling effect, and interfacial charge-transfer effect provide a physically reasonable interpretation for the stronger near-field response observed in Fig. 3d.

Experimental results further verified the sensitivity-enhancement trend revealed by the simulation (Fig. S1). For bare-Au SPR, the reflectance curves shift with increasing refractive index over n = 1.3320, 1.3385, 1.3435, 1.3472 and 1.3530, and linear fitting gives an angular sensitivity of 132 deg/RIU (Fig. S1a, c). After formation of the 13 nm BP-COOH functional layer, the resonance-angle displacement becomes clearly larger over the same refractive-index range, and the corresponding angular sensitivity increases to 281 deg/RIU (Fig. S1b, c). Thus, the experimental results show the same enhancement trend as the simulation results.

Taken together, Fig. 3, Fig. 4 and Fig. S1 show that introducing the BP overlayer strengthens the interfacial optical response of the Au-film SPR structure to refractive-index variation. The simulation results establish the sensitivity-enhancement trend, the schematic in Fig. 4 provides a physical interpretation of the enhanced near-field response, and the refractive-index experiments verify the same trend experimentally. These results provide the optical basis for the subsequent improvement in Pb^{2+} sensing performance observed for SPR + BP-COOH.

Pb^{2+} sensing performance and specificity of SPR + BP-COOH. The Pb^{2+} sensing performance of SPR + BP-COOH is summarized in Fig. 5. As shown in Fig. 5a, when the Pb^{2+} concentration increases from 0 to 10^{-15} M, the angle-scanned reflectance curves of SPR + BP-COOH exhibit clear and concentration-dependent resonance-angle shifts over the entire tested range. Notably, a distinguishable response is already observed at 10^{-19} M. In contrast, the corresponding bare-Au SPR curves remain unresolved within the same low-concentration range, indicating that the introduction of the BP-COOH functional layer markedly extends the detectable Pb^{2+} concentration regime toward much lower concentrations. On the basis of distinguishable reflectance curves, the LOD of SPR + BP-COOH reaches 10^{-19} M.

The concentration dependence of the resonance-angle response is further summarized in Fig. 5b. For SPR + BP-COOH, the resonance-angle shift $\Delta\theta$ increases monotonically with increasing Pb^{2+} concentration, and the fitted curve clearly extends into the ultralow-concentration regime. Under the same sensing framework, bare-Au SPR only begins to show distinguishable Pb^{2+} responses at much higher concentrations, and its LOD is 10^{-6} M. The corresponding angle-scanned reflectance curves and fitting results for bare-Au SPR are provided in Fig. S5. Therefore, relative to bare-Au SPR, the BP-COOH

functional layer shifts the detectable Pb^{2+} concentration regime by 13 orders of magnitude on the same optical platform.

To further examine the reliability of this ultralow-concentration response, several control and validation experiments were performed. First, after deposition of the BP-COOH functional layer, repeated measurements of pure water at 2 min intervals show that the reflectance curves remain nearly unchanged, with instrumental fluctuation within 20 mdeg (Fig. S11). This indicates that the low-concentration angle shifts observed in Fig. 5a are beyond the instrumental drift range. Second, repeated measurements performed on the same 13 nm SPR + BP-COOH structure again show distinguishable Pb^{2+} responses at 10^{-19} M, and the corresponding Δθ–concentration relationship remains monotonic (Fig. S2). Third, different-thickness validation using an approximately 11 nm SPR + BP-COOH structure also retains a distinguishable response at 10^{-19} M (Fig. S3). These results together support the robustness of the 10^{-19} M Pb^{2+} response in the present sensing strategy.

The specificity of SPR + BP-COOH was further evaluated by comparing its responses to other divalent metal ions. As shown in Fig. 5b, the round symbols correspond to the Δθ values of SPR + BP-COOH for different ions, whereas the square symbols represent the bare-Au SPR response to Pb^{2+}. Among all tested ions, Pb^{2+} exhibits the lowest distinguishable concentration. The LODs for the other metal ions are 10^{-13} M for Cd^{2+}, 10^{-13} M for Cu^{2+}, 10^{-12} M for Zn^{2+}, 10^{-10} M for Ni^{2+}, 10^{-9} M for Ca^{2+}, and 10^{-8} M for Mg^{2+}. Thus, although SPR + BP-COOH also responds to these ions at sufficiently high concentrations, its response to Pb^{2+} appears in a substantially lower concentration regime than those of Cd^{2+}, Cu^{2+}, Zn^{2+}, Ni^{2+}, Ca^{2+}, and Mg^{2+} under identical measurement conditions. The corresponding angle-scanned reflectance curves and nonlinear fitting results for Cd^{2+}, Cu^{2+}, Zn^{2+}, Ni^{2+}, Ca^{2+}, and Mg^{2+} are provided in Figs. S5-10.

The detailed Δθ values for SPR + BP-COOH at different ion concentrations are listed in Fig. 5c. These data further show that the Pb^{2+} response is initiated at much lower concentration than the responses to the other tested ions, in agreement with the fitted trends in Fig. 5b. Taken together, Fig. 5 establishes the sensing performance of SPR + BP-COOH from three aspects. First, SPR + BP-COOH enables distinguishable Pb^{2+} detection down to 10^{-19} M, whereas bare-Au SPR only reaches 10^{-6} M. Second, this ultralow-concentration response is supported by instrumental-stability control, repeatability on the same 13 nm structure, and different-thickness validation. Third, the detectable concentration regime for Pb^{2+} remains markedly lower than those of Cd^{2+}, Cu^{2+}, Zn^{2+}, Ni^{2+}, Ca^{2+}, and Mg^{2+}, demonstrating the specificity of the BP-COOH functional layer toward Pb^{2+} within the present sensing system.

Comparison with representative Pb^{2+} sensing strategies. To position the present sensing performance in the context of reported Pb^{2+} detection technologies, the LOD of SPR + BP-COOH was compared with representative studies from four categories, including SPR sensors, fluorescent probes, colorimetric/LSPR probes, and electrochemical/PEC biosensors, as summarized in Fig. 6. Within the representative SPR studies, previously reported LODs span from 4.8×10^{-9} M to 5.0×10^{-15} M, including 4.8×10^{-9} M for a fiber-based SPR sensor [19], 8.0×10^{-11} M for a label-free SPR platform based on

DNAzyme-gold nanoparticle conjugates [17], and 5.0 × 10^{-15} M for an amplified SPR format using a Pb^{2+}-dependent DNAzyme and a hemin/G-quadruplex label [20]. Representative fluorescent probes reported LODs of 4.8 × 10^{-8} M, 9.6 × 10^{-11} M, and 3.8 × 10^{-9} M [9,10,33]. Representative colorimetric/LSPR probes reported LODs in the range of 1.0 × 10^{-7} to 2.4 × 10^{-12} M [18,34–37]. Representative electrochemical and PEC biosensors further reached 1.5 × 10^{-11} M, 1.67 × 10^{-14} M, 1.26 × 10^{-15} M, 1.67 × 10^{-11} M, and 7.0 × 10^{-17} M, respectively [11–13,38,39].

Against this representative literature background, the LOD of SPR + BP-COOH reaches 10^{-19} M, placing the present work in a distinctly lower concentration regime than the compared SPR, fluorescent, colorimetric/LSPR, and electrochemical/PEC reports shown in Fig. 6. This comparison is notable because the present platform is still based on a prism-coupled Au-film SPR configuration rather than on multistep amplified electrochemical readout. In other words, the performance gain is achieved by direct interfacial engineering of the sensing layer on a traditional SPR platform. Together with the results in Fig. 1–4, this comparison shows that the BP-COOH functional layer enables a substantial extension of the detectable Pb^{2+} concentration regime while retaining the label-free optical readout format of SPR.

Discussion

In summary, we constructed a surface plasmon resonance sensor modified with carboxyl-functionalized BP (SPR + BP-COOH) and demonstrated its ultralow-concentration Pb^{2+} sensing capability on a prism-coupled Au-film SPR platform. The BP-COOH functional layer provides oxygen-containing interfacial sites for Pb^{2+} interaction, while also enhancing the optical response of the SPR interface. This combination is supported by the interfacial characterization, the simulation results, and the refractive-index-dependent experimental response. As a result, SPR + BP-COOH enables distinguishable Pb^{2+} detection down to 10^{-19} M, whereas bare-Au SPR only reaches 10^{-6} M under the same sensing framework.

In addition to the markedly extended detectable concentration regime, SPR + BP-COOH also exhibits a substantially lower response range for Pb^{2+} than for Cd^{2+}, Cu^{2+}, Zn^{2+}, Ni^{2+}, Ca^{2+}, and Mg^{2+}. The instrumental-stability test, repeated measurements on the same 13 nm structure, and different-thickness validation further support the reliability of this sensing strategy. Overall, this work shows that direct interfacial engineering with a BP-COOH functional layer can substantially improve the performance of conventional label-free SPR for Pb^{2+} detection. These results provide a simple route for extending traditional Au-film SPR toward ultratrace heavy-metal-ion sensing.

Methods

Materials

Carboxyl-functionalized BP (BP-COOH) was purchased from Xi'an Ruixi Biological Technology and used as the sensing material. Pb, Cd, Cu, Zn, Ni, Ca and Mg standard single-element solutions were used for ion sensing experiments. The Pb standard solution was GSB 04-1742-2004 (1000 μg/mL, c(HNO_3) = 1.0

mol/L). The Cd, Cu, Zn, Ni, Ca and Mg standard solutions were GSB 04-1721-2004, GSB 04-1725-2004, GSB 04-1761-2004, GSB 04-1740-2004, GSB 04-1720-2004 and GSB 04-1735-2004, respectively, all with a standard value of 1000 μg/mL in c(HNO_3) = 1.0 mol/L medium. Pure water was used for sample preparation and sensing measurements. Unless otherwise specified, all experimental procedures were carried out in a clean laboratory.

Preparation of BP-COOH

Commercial BP-COOH was obtained from Xi'an Ruixi Biological Technology, and its preparation route is described as follows. BP nanosheets were prepared by liquid-phase exfoliation. Specifically, 5 g NaOH was added into 50 mL anhydrous N-methyl-2-pyrrolidone (NMP) and sonicated in a water bath at 180 W for 30 min to obtain alkalized NMP. Bulk BP crystals were then dispersed into the alkalized NMP solution and ultrasonicated at 500 W in an ice bath using a pulse sequence of 3 s on and 3 s off, while the probe temperature was kept below 40°C. The sonication was continued for 8–10 h. The resulting dispersion was first centrifuged at 4000 rpm at 4°C for 10 min, and the supernatant was collected. The collected supernatant was then centrifuged at 13200 rpm at 4°C for 15–20 min, and the precipitate was collected as BP nanosheets.

For carboxyl functionalization, the concentration of the BP nanosheet dispersion was adjusted to 1 mg/mL. Then, 2.5 mg PEI aqueous solution (500 μL) was added, and the mixture was stirred at 500 rpm in a brown bottle under light protection overnight to obtain amino-functionalized BP nanosheets. Subsequently, 2 mL poly(acrylic acid) (PAA, molecular weight 5000, 50%) was adjusted to approximately pH 7.0 by adding 5 mol NaOH stepwise under pH-meter monitoring, and then added dropwise into the above dispersion under magnetic stirring. The mixture was further stirred at room temperature for 6 h, followed by centrifugation, washing with water 2–3 times, and redispersion in deionized water to obtain BP-COOH. A freeze-drying protectant was then added at 20 times the mass of the BP nanosheets. The resulting dispersion was frozen at − 80°C for 24 h and then freeze-dried for 72 h.

Fabrication of SPR + BP-COOH

BP-COOH was stored at − 20°C under light protection before use. For sensing experiments, 0.0001 g BP-COOH was dispersed in 1 mL pure water in the clean laboratory and sonicated in an ice-water bath for 480 s. The dispersion was freshly prepared before use.

The SPR substrate consisted of a 50 nm Au film with a 5 nm Cr adhesion layer. Before use, the Au-coated chip was rinsed once with ethanol, once with pure water and once again with ethanol. For fabrication of SPR + BP-COOH, 0.5 mL of the freshly prepared BP-COOH dispersion was drop-cast onto the Au film and dried naturally at 25°C in the clean laboratory. The main-text 13 nm structure and the 11 nm structure used for different-thickness validation were prepared in the same way, and the thickness difference arose from deposition variation. During assembly of the SPR device, cedar wood oil (MACKLIN, C805296) was used as the refractive-index-matching medium between the Au chip and the BK7 prism.

SPR measurements

SPR measurements were performed on a Dynechem SPR system using 633 nm incident light at 25°C. The angular scanning range was 65°–80°, and the angular step was 19–21 mdeg. For each measurement, 400 μL of sample solution was introduced onto the sensing interface, and the signal was collected after 30 s. The resonance-angle shift Δθ was defined relative to pure water (0 M). The instrumental fluctuation was within ± 20 mdeg, determined from the maximum drift of repeated pure-water measurements.

For the repeatability test, the same 13 nm SPR + BP-COOH structure was remeasured from pure water to increasing Pb^{2+} concentrations. For different-thickness validation, the same sensing procedure was applied to the approximately 11 nm SPR + BP-COOH structure. For the bare-Au SPR control, Pb^{2+} solutions were measured directly on the Au film without BP-COOH deposition.

Preparation of ion solutions

All ion solutions were prepared in the clean laboratory. The purchased single-element standard solutions were first converted to 10^{-2} M stock solutions and then diluted stepwise by a factor of 10 using pure water to obtain the required concentration series. The pH of the test solutions remained at 6.3, and all ions were measured under the same matrix conditions. For ultralow-concentration dilution, a new container and a new pipette tip were used at each dilution step.

Definition of LOD

The LOD was defined as the lowest concentration at which the reflectance curve became distinguishable beyond the instrumental drift range. When the response of the ion solution exceeded the instrumental error range, that concentration was considered distinguishable and was taken as the LOD.

AFM characterization

AFM measurements were performed on a Bruker Dimension Icon instrument in ScanAsyst mode using a SCANASYST-AIR probe. The probe was made of SiN and had a resonance frequency of 70 kHz, a tip height of 2.5–8 μm, a typical curvature radius of 2 nm, a cantilever length of 115 μm, a cantilever thickness of 0.65 μm, a width of 35 μm and a spring constant of 0.4 N/m. The scanning frequency was 1 Hz.

XPS characterization

XPS measurements were performed on a ThermoFisher K-Alpha+ system using an Al Kα X-ray source. The pass energy was 100 eV for survey spectra and 50 eV for high-resolution spectra. The chamber pressure was 4.1E − 9 mBar before analysis and 3.9E − 7 mBar during analysis. Charge correction was referenced to C 1s at 284.8 eV. Background subtraction was performed using the smart method.

STEM-EDS characterization

STEM measurements were performed on a JEOL JEM-F200 transmission electron microscope operated at 200 kV. The instrument was used at a high-resolution magnification up to 1.5 million. EDS analysis was performed using a JEOL JED-2300T system.

Simulation

The optical response of the SPR structure was calculated by the transfer matrix method (TMM) [32]. The incident wavelength was set to 633 nm. The refractive index of the BK7 prism was taken as 1.5151 [29,40]. The thickness of a single BP layer was taken as 0.53 nm, and its refractive index was taken as 3.5 + 0.01i [29,41]. The Au thickness was 50 nm, and its refractive index was calculated by the Drude model as 0.1378 + 3.6195i [42]. The angular sensitivity was defined as the resonance-angle change divided by the refractive-index change.

Declarations

Acknowledgements

This work is partially supported by the National Natural Science Foundation of China (Grant No. 62475049), the Guangzhou Municipal Science and Technology Bureau Technology Development Program (Grant No. 2024A04J6315).

References

1. Hou D et al (2025) Global soil pollution by toxic metals threatens agriculture and human health. Science 388:316–321
2. Hou D et al (2020) Metal contamination and bioremediation of agricultural soils for food safety and sustainability. Nat Reviews Earth Environ 1:366–381
3. Chen M et al (2025) Environmental lead risk in the 21st century. Commun Earth Environ 6:776
4. Wei R et al (2023) Heavy metal concentrations in rice that meet safety standards can still pose a risk to human health. Commun Earth Environ 4:84
5. Landrigan PJ, Bellinger D (2021) It’s time to end lead poisoning in the United States. JAMA Pediatr 175:1216–1217
6. Lanphear B, Navas-Acien A, Bellinger DC (2024) Lead poisoning. N Engl J Med 391:1621–1631
7. McFarland MJ, Hauer ME, Reuben A (2022) Half of US population exposed to adverse lead levels in early childhood. Proceedings of the National Academy of Sciences 119, e2118631119
8. Ciccarelli D et al (2025) Bridging knowledge gaps in human chemical exposure via drinking water with non-target screening. Crit Rev Environ Sci Technol 55:190–214

9. Zhang Y et al (2018) Simultaneous detection of trace toxic metal ions, Pb^{2+} and Ag^{+}, in water and food using a novel single-labeled fluorescent oligonucleotide probe. Sens Actuators B 261:58–65
10. Lee JY et al (2023) Development of ratiometric fluorescent probes based on peptides for sensing Pb^{2+} in aquatic environments and human serum. Spectrochim Acta Part A Mol Biomol Spectrosc 294:122502
11. Meng J et al (2021) A single-step DNAzyme sensor for ultra-sensitive and rapid detection of Pb^{2+} ions. Electrochim Acta 368:137551
12. Li M et al (2024) An electrochemical biosensor with homogeneous dual amplification strategy for sensitive analysis of Pb^{2+}. Sens Actuators B 418:136225
13. Li M et al (2025) Bi_2WO_6-based photoelectrochemical biosensor with DNAzyme-assisted amplification strategy for Pb^{2+} analysis. Microchem J 115393
14. Liedberg B, Nylander C, Lunström I (1983) Surface plasmon resonance for gas detection and biosensing. Sens Actuators 4:299–304
15. Homola J (2008) Surface plasmon resonance sensors for detection of chemical and biological species. Chem Rev 108:462–493
16. Hojjat Jodaylami M, Masson J-F, Badia A (2025) Surface plasmon resonance sensing. Nat Reviews Methods Primers 5:47
17. Wu H et al (2020) A label-free lead (II) ion sensor based on surface plasmon resonance and DNAzyme-gold nanoparticle conjugates. Anal Bioanal Chem 412:7525–7533
18. Amirjani A et al (2022) SPR-based assay kit for rapid determination of Pb^{2+}. Anal Chim Acta 1220:340030
19. Suhailin FH et al (2020) Fiber-based surface plasmon resonance sensor for lead ion detection in aqueous solution. Plasmonics 15:1369–1376
20. Pelossof G, Tel-Vered R, Willner I (2012) Amplified surface plasmon resonance and electrochemical detection of Pb^{2+} ions using the Pb^{2+}-dependent DNAzyme and hemin/G-quadruplex as a label. Anal Chem 84:3703–3709
21. Sharely I et al (2025) Unleashing the Biosensing Potential of 2D Inorganic Nanomaterials: the Journey of a Decade. Chem – Eur J 31:e202501080
22. Liu L et al (2021) Grain-boundary-rich polycrystalline monolayer WS_2 film for attomolar-level Hg^{2+} sensors. Nat Commun 12:3870
23. Zhang W et al (2024) High-Active Surface of Centimeter-Scale β-In_2S_3 for Attomolar-Level Hg^{2+} Sensing. Nano Lett 24:12684–12690
24. Li L et al (2014) Black phosphorus field-effect transistors. Nat Nanotechnol 9:372–377
25. Wei J et al (2025) The Progress of Black Phosphorus in the Field of Sensors. Crit Rev Anal Chem 1–27
26. Liu X et al (2020) Regulating the reactivity of black phosphorus via protective chemistry. Sci Adv 6:eabb4359

27. Yadav PK et al (2024) 2D material–based surface plasmon resonance biosensors for applications in different domains: an insight. Microchim Acta 191:373
28. Cui S et al (2015) Ultrahigh sensitivity and layer-dependent sensing performance of phosphorene-based gas sensors. Nat Commun 6:8632
29. Wu L et al (2017) Sensitivity enhancement by using few-layer black phosphorus-graphene/TMDCs heterostructure in surface plasmon resonance biochemical sensor. Sens Actuators B 249:542–548
30. Wang S et al (2024) A library of 2D electronic material inks synthesized by liquid-metal-assisted intercalation of crystal powders. Nat Commun 15:6388
31. Peng Q et al (2014) Unique lead adsorption behavior of activated hydroxyl group in two-dimensional titanium carbide. J Am Chem Soc 136:4113–4116
32. Hansen WN (1968) Electric fields produced by the propagation of plane coherent electromagnetic radiation in a stratified medium. J Opt Soc Am 58:380–390
33. Marbella L, Serli-Mitasev B, Basu P (2009) Development of a fluorescent Pb^{2+} sensor. Angew Chem 121:4056–4058
34. Chai F et al (2010) Colorimetric detection of Pb^{2+} using glutathione functionalized gold nanoparticles. ACS Appl Mater Interfaces 2:1466–1470
35. Thatai S et al (2016) Trace colorimetric detection of Pb^{2+} using plasmonic gold nanoparticles and silica–gold nanocomposites. Microchem J 124:104–110
36. Xie M-R et al (2020) Sensitive colorimetric detection of Pb^{2+} by geometric field amplification and surface plasmon resonance visualization. Talanta 212:120749
37. Mohammadi F et al (2025) Label-free colorimetric biosensor for sensitive detection of lead (II) ion based on aptazyme-amplified oxidase-like activity of MnO_2 nanoflowers. Biosens Bioelectron 287:117751
38. Lai C et al (2019) Electrochemical biosensor for amplified detection of Pb^{2+} based on perfect match of reduced graphene oxide–gold nanoparticles and single-stranded DNAzyme. Anal Bioanal Chem 411:7499–7509
39. Li J et al (2024) Novel nucleic acid-assisted ion-responsive ECL biosensor based on hollow AuAg nanoboxes with excellent SPR and effective coreaction acceleration. Anal Chem 96:11076–11082
40. Zeng S et al (2015) Graphene–MoS_2 hybrid nanostructures enhanced surface plasmon resonance biosensors. Sens Actuators B 207:801–810
41. Mao N et al (2016) Optical anisotropy of black phosphorus in the visible regime. J Am Chem Soc 138:300–305
42. Xue T, Qi K, Hu C (2019) Novel SPR sensing platform based on superstructure MoS_2 nanosheets for ultrasensitive detection of mercury ion. Sens Actuators B 284:589–594

Figures

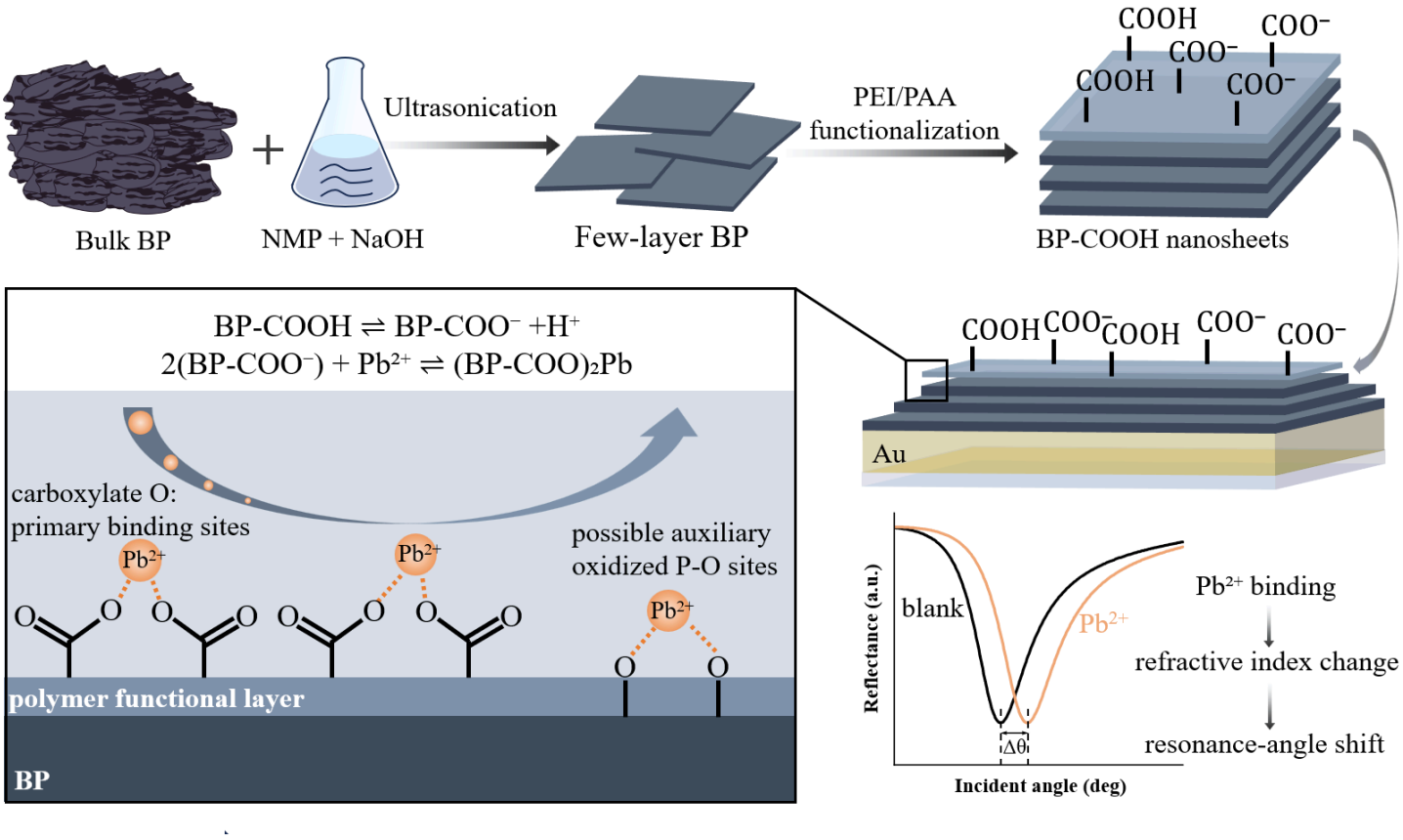


Figure 1

Preparation of BP-COOH nanosheets, construction of built-in electric field-enhanced SPR+BP-COOH, and schematic illustration of the proposed Pb^{2+} recognition pathway. Bulk BP was exfoliated in NMP + NaOH to obtain few-layer BP, followed by PEI/PAA functionalization to form BP-COOH nanosheets. The BP-COOH nanosheets were then deposited onto the Au film to construct SPR+BP-COOH. The lower schematic shows the proposed interaction of Pb^{2+} with oxygen-containing sites in the BP-COOH functional layer and the corresponding resonance-angle shift induced by interfacial refractive-index change.

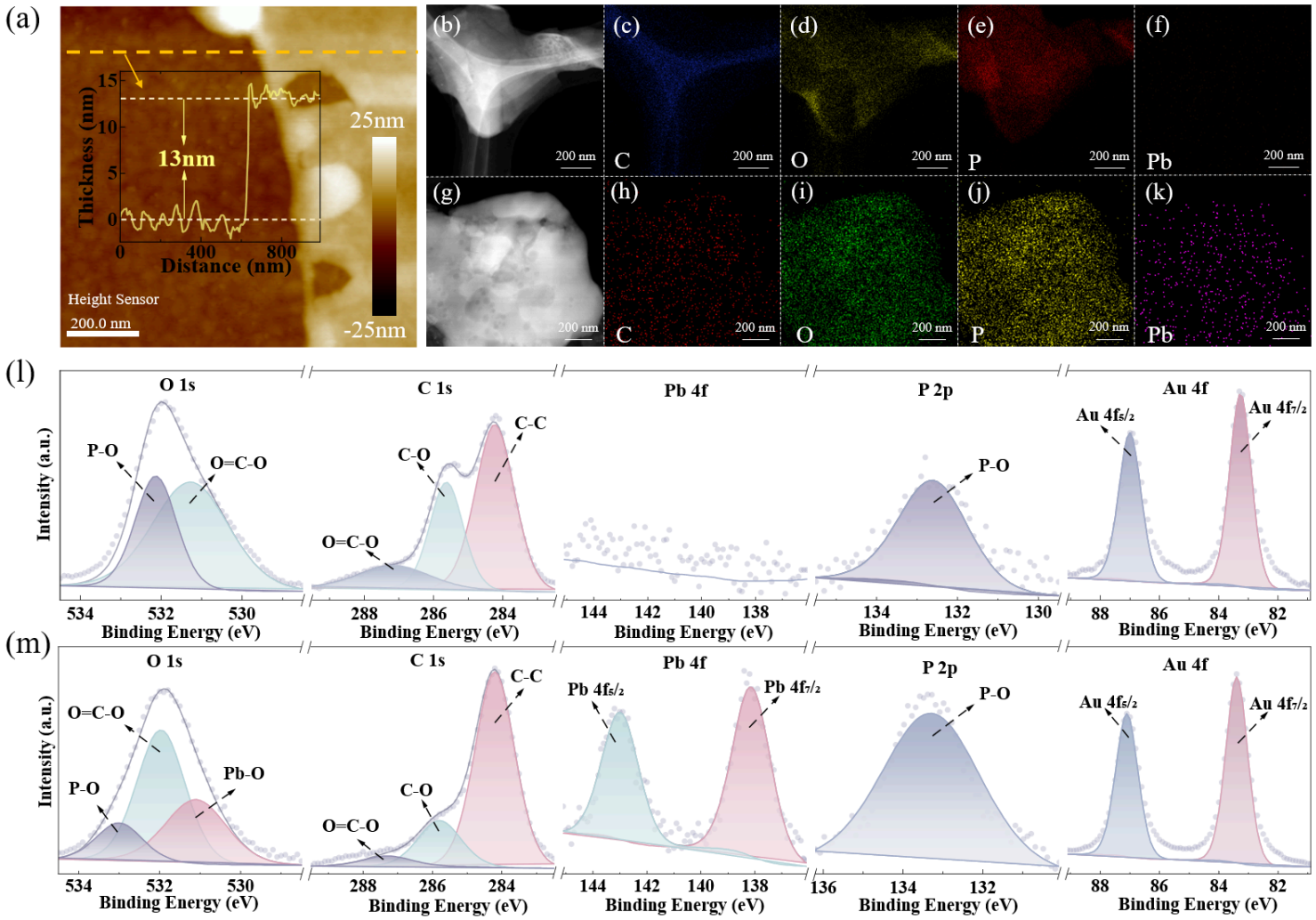


Figure 2

AFM, STEM image, EDS elemental maps, and XPS characterization of the SPR+BP-COOH interface before and after Pb^{2+} exposure. (a)AFM image and height profile of the BP-COOH functional layer on the Au film, showing a thickness of approximately 13 nm. **(b)** STEM image of the BP-COOH functional layer before Pb^{2+} exposure. **(c–f)** Corresponding EDS elemental maps of C, O, P, and Pb before Pb^{2+} exposure. **(g)** STEM image of the BP-COOH functional layer after Pb^{2+} exposure. **(h–k)** Corresponding EDS elemental maps of C, O, P, and Pb after Pb^{2+} exposure. **(l)** XPS spectra of O 1s, C 1s, Pb 4f, P 2p, and Au 4f before Pb^{2+} exposure. **(m)**XPS spectra of O 1s, C 1s, Pb 4f, P 2p, and Au 4f after Pb^{2+} exposure.

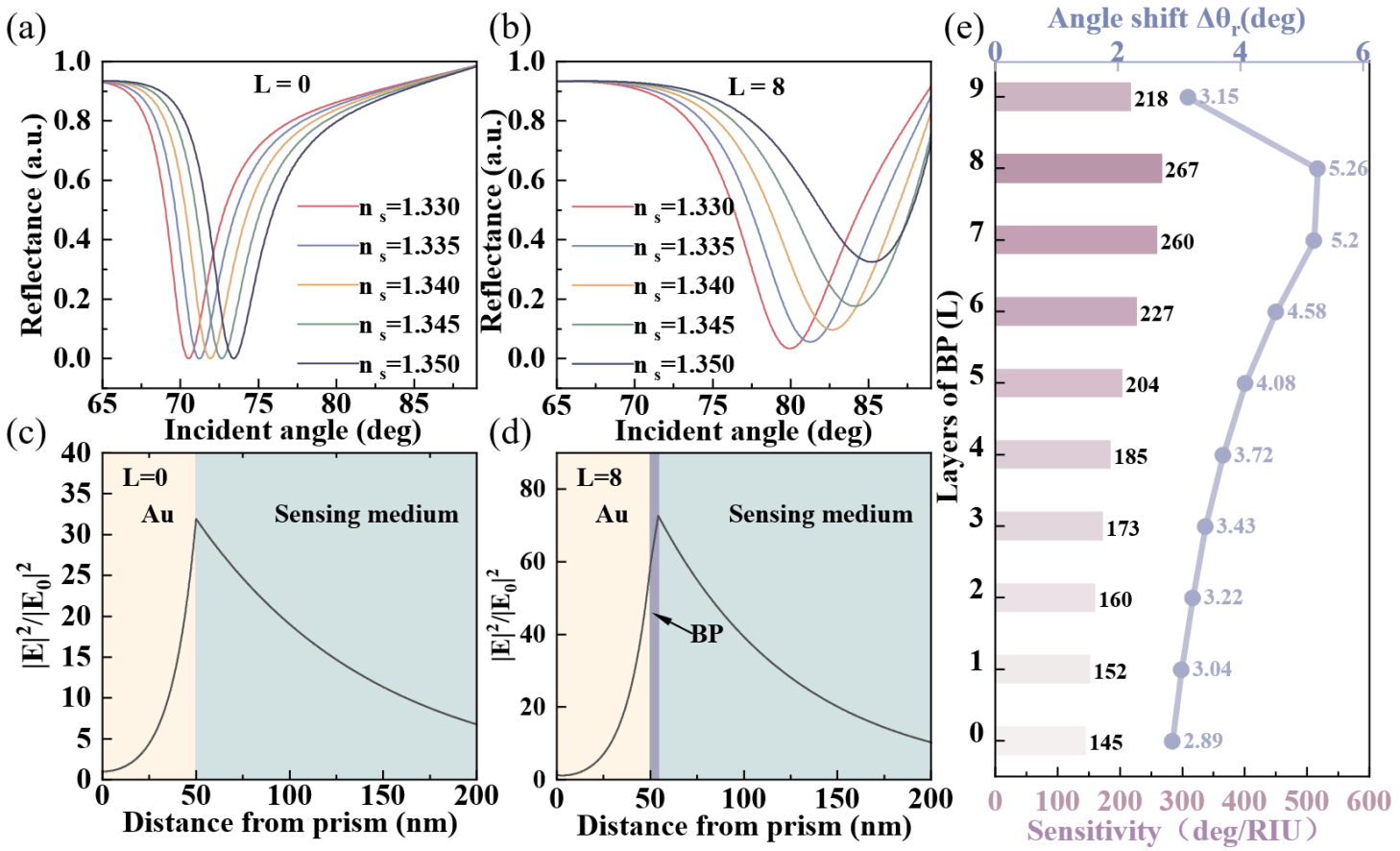


Figure 3

Simulated angular SPR response, electric-field distribution, and layer-number-dependent sensitivity of the Au-film SPR structure with and without a BP overlayer. (a) Simulated angle-scanned reflectance curves of bare-Au SPR with L = 0 at sensing-medium refractive indices n = 1.330, 1.335, 1.340, 1.345, and 1.350. **(b)** Simulated angle-scanned reflectance curves of the BP-modified SPR structure with L = 8 at sensing-medium refractive indices n = 1.330, 1.335, 1.340, 1.345, and 1.350. **(c)** Normalized electric-field intensity distribution of the bare-Au SPR structure with L = 0. **(d)**Normalized electric-field intensity distribution of the BP-modified SPR structure with L = 8. **(e)** Simulated angular sensitivity and total resonance-angle shift as a function of the number of BP layers.

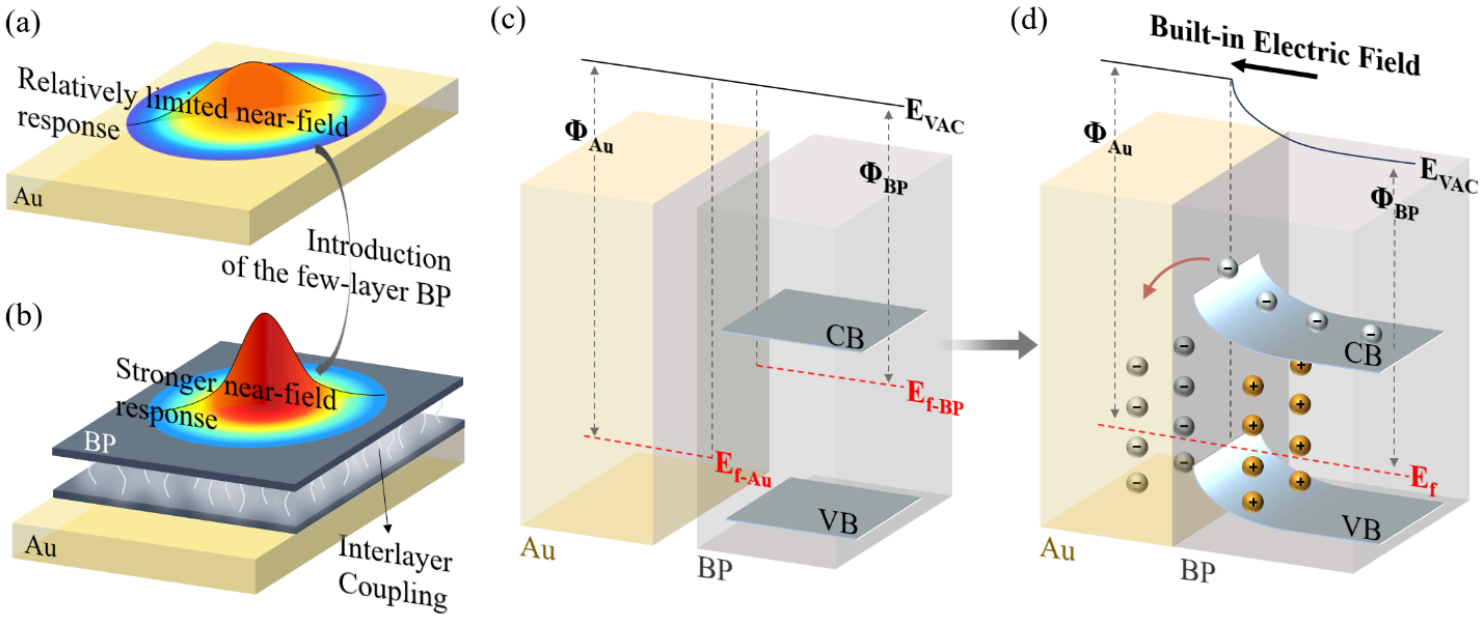


Figure 4

Schematic physical interpretation of BP-enhanced near-field response at the SPR interface. (a) Schematic near-field distribution at the Au/sensing-medium interface, showing a relatively limited near-field response. **(b)** Schematic near-field distribution after introduction of the BP overlayer, showing enhanced field confinement and a stronger near-field response; interlayer coupling within the multilayer BP structure is also illustrated. **(c)** Schematic energy-level alignment of Au and BP before interfacial charge redistribution, showing the work functions and band positions of the two components. **(d)** Schematic interfacial charge-transfer process after Au/BP contact, showing the formation of a built-in electric field and the resulting enhancement of local field coupling at the interface.

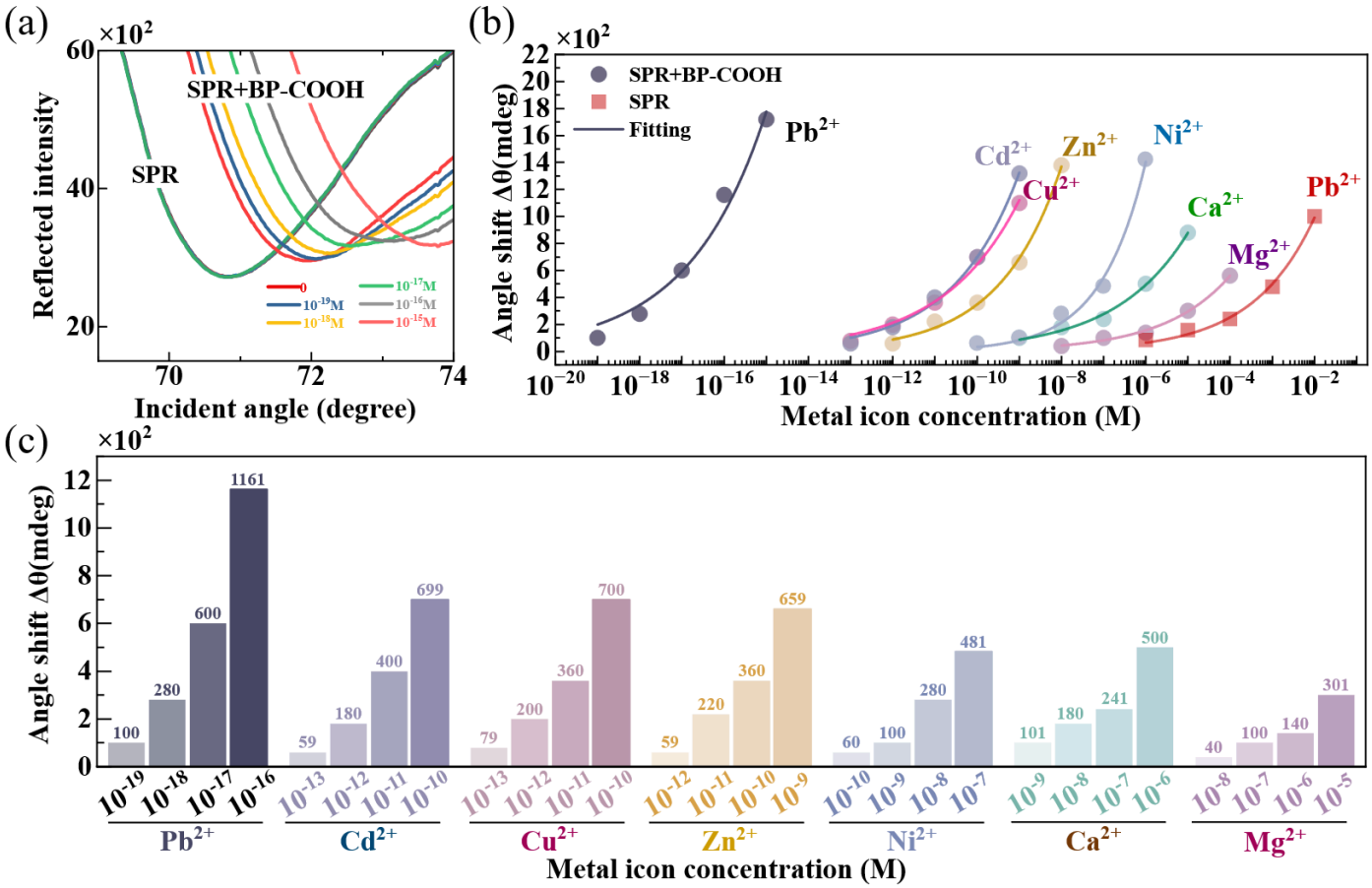


Figure 5

Pb²⁺ sensing response of SPR+BP-COOH and comparison with other metal ions and bare-Au SPR. (a) Angle-scanned reflectance curves of SPR+BP-COOH measured for Pb²⁺ concentrations of 0, 10^{-19}, 10^{-18}, 10^{-17}, 10^{-16} and 10^{-15} M, together with the reflectance curve of bare-Au SPR. **(b)** Resonance-angle shift Δθ as a function of metal-ion concentration for SPR+BP-COOH and bare-Au SPR. Round symbols represent SPR+BP-COOH, square symbols represent bare-Au SPR, and solid lines represent nonlinear fitting curves. **(c)** Resonance-angle shift Δθ values of SPR+BP-COOH measured at different concentrations of Pb²⁺, Cd²⁺, Cu²⁺, Zn²⁺, Ni²⁺, Ca²⁺ and Mg²⁺.

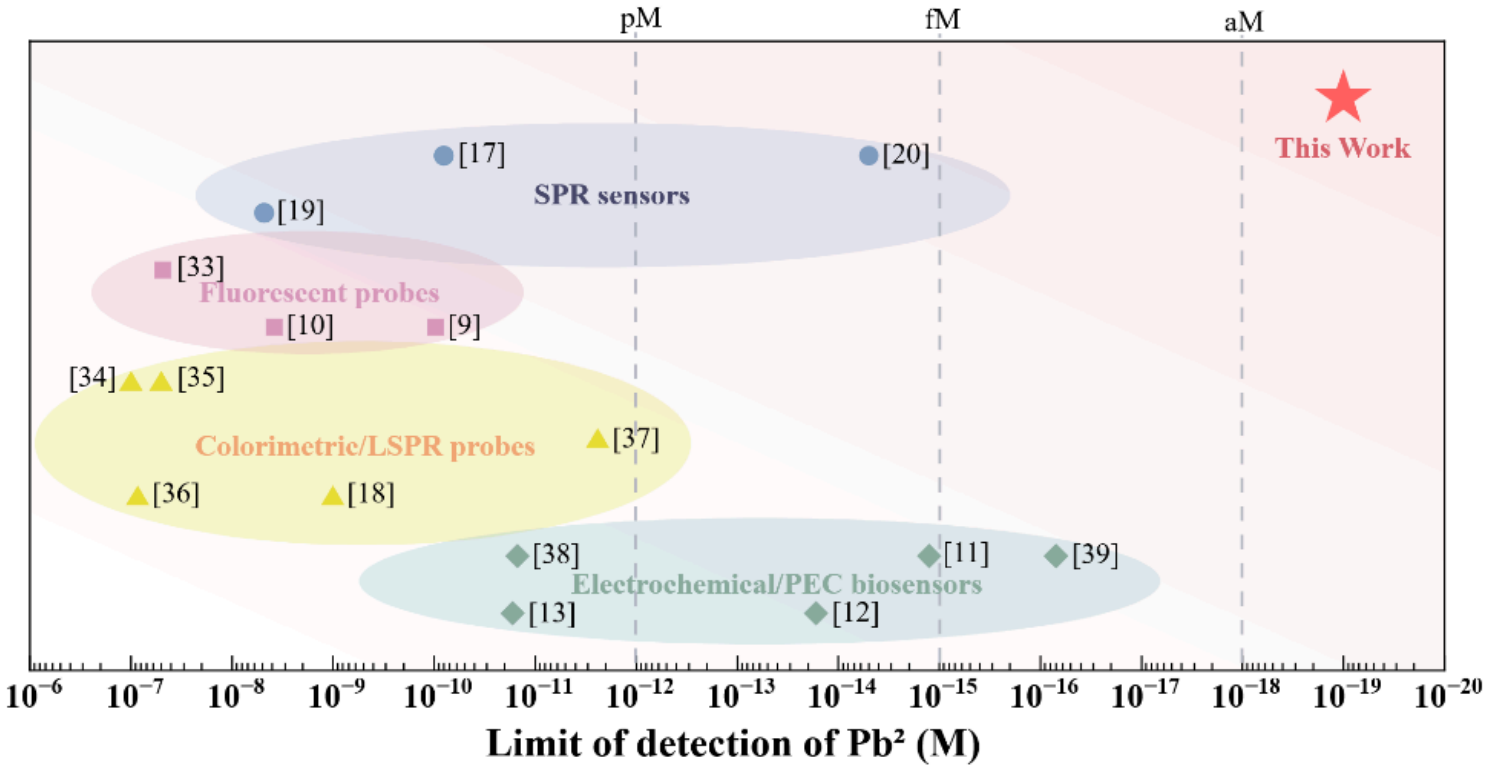


Figure 6

Comparison of the Pb^{2+} LOD of this work with representative reports from four sensing categories. LOD values from representative SPR sensors, fluorescent probes, colorimetric/LSPR probes, and electrochemical/PEC biosensors are plotted on the concentration axis, together with the result of this work. The corresponding references are [9–13,17–20,33–39].

Supplementary Files

This is a list of supplementary files associated with this preprint. Click to download.

- SourceData.xlsx
- SupportingInformation.docx
- SupportingInformation.docx